

RESEARCH ARTICLE

10.1002/2017JA024311

Density Structures, Dynamics, and Seasonal and Solar Cycle Modulations of Saturn's Inner Plasma Disk

Key Points:

- The plasma density of the inner plasma disk of Saturn shows a solar EUV flux dependency
- The ion density measured between 4 and 5 R_S shows a clear dayside/nightside asymmetry
- The plasma disk peak density is shifted $\sim 0.6 R_S$ out from the main source, due to hot electron impact ionization

Correspondence to:

M. K. G. Holmberg
mika.holmberg@irap.omp.eu

Citation:

Holmberg, M. K. G., Shebanits, O., Wahlund, J.-E., Morooka, M. W., Vigrén, E., André, N., ... Gilbert, L. K. (2017). Density structures, dynamics, and seasonal and solar cycle modulations of Saturn's inner plasma disk. *Journal of Geophysical Research: Space Physics*, 122, 12,258–12,273. <https://doi.org/10.1002/2017JA024311>

Received 27 APR 2017

Accepted 15 NOV 2017

Accepted article online 20 NOV 2017

Published online 22 DEC 2017

M. K. G. Holmberg^{1,2,3} , O. Shebanits^{1,2} , J.-E. Wahlund^{1,2} , M. W. Morooka¹, E. Vigrén¹, N. André³ , P. Garnier³ , A. M. Persoon⁴ , V. Génot³, and L. K. Gilbert⁵ 

¹Swedish Institute of Space Physics, Uppsala, Sweden, ²Department of Physics and Astronomy, Uppsala University, Uppsala, Sweden, ³IRAP, University of Toulouse, CNRS, UPS, CNES, Toulouse, France, ⁴Department of Physics and Astronomy, University of Iowa, Iowa City, IA, USA, ⁵Mullard Space Science Laboratory, University College London, Dorking, UK

Abstract We present statistical results from the Cassini Radio and Plasma Wave Science (RPWS) Langmuir probe measurements recorded during the time interval from orbit 3 (1 February 2005) to 237 (29 June 2016). A new and improved data analysis method to obtain ion density from the Cassini LP measurements is used to study the asymmetries and modulations found in the inner plasma disk of Saturn, between 2.5 and 12 Saturn radii ($1 R_S = 60,268$ km). The structure of Saturn's plasma disk is mapped, and the plasma density peak, n_{\max} , is shown to be located at $\sim 4.6 R_S$ and not at the main neutral source region at $3.95 R_S$. The shift in the location of n_{\max} is due to that the hot electron impact ionization rate peaks at $\sim 4.6 R_S$. Cassini RPWS plasma disk measurements show a solar cycle modulation. However, estimates of the change in ion density due to varying EUV flux is not large enough to describe the detected dependency, which implies that an additional mechanism, still unknown, is also affecting the plasma density in the studied region. We also present a dayside/nightside ion density asymmetry, with nightside densities up to a factor of 2 larger than on the dayside. The largest density difference is found in the radial region 4 to 5 R_S . The dynamic variation in ion density increases toward Saturn, indicating an internal origin of the large density variability in the plasma disk rather than being caused by an external source origin in the outer magnetosphere.

1. Introduction

Cassini is the first spacecraft with the main objective to study the Saturnian system during a long-term mission. The spacecraft went into orbit around Saturn on 30 June 2004, and the mission ended on 15 September 2017 when the spacecraft entered into the atmosphere of Saturn and was destroyed. Before the end of the mission most of its instruments were still, more than 13 years after the orbit insertion, in an excellent state of health. Among them was the Cassini Langmuir probe (LP), part of the Radio and Plasma Wave Science (RPWS) instrument package. Hence, around 13 years of RPWS/LP in situ measurements of Saturn's space environment are available for analyses. In this article we use a data set spanning over ~ 11.5 years to study the structure and dynamics and the solar cycle and seasonal modulations of the plasma located between 2.5 and 12 Saturn radii ($1 R_S = 60,268$ km) from Saturn.

The inner plasma disk of Saturn is created from material originating from the plumes of the moon Enceladus. Cassini measurements have shown that Enceladus is feeding its environment with new material, venting from plumes located in the moon's south polar region (e.g., Dougherty et al., 2006; Porco et al., 2006). These geysers consist mainly of water vapor and condensed water. As the expelled neutrals are ionized, by electron impact ionization and photoionization, and transported away, a plasma disk is created in the region around the orbit of Enceladus. The main ion components in the inner plasma disk are hydrogen ions H^+ and water group ions W^+ (O^+ , OH^+ , H_2O^+ , and H_3O^+).

The Cassini Saturn Orbit Insertion provided many estimates of the properties of the plasma disk, such as the plasma density and temperature, ion composition, azimuthal ion velocity, and average ion mass (e.g., Gurnett et al., 2005; Moncuquet et al., 2005; Sittler Jr. et al., 2006, 2008; Wahlund et al., 2005; Young et al., 2005). As the mission progressed the growing data sets provided new and more accurate results and the possibility to perform statistical analyses. Persoon et al. (2005) used upper hybrid resonance emission measurements to derive the electron density, n_e , for five equatorial orbits. They presented equatorial density profiles

with a highly repeatable radial dependence, which was well described by $R^{-3.63}$ where R is the radial distance in R_S from the center of Saturn, for distances larger than $5 R_S$. Inside $5 R_S$ the presented electron density profiles were shown to be highly variable. A study of the ion plasma parameters was presented by Thomsen et al. (2010), who used roughly 4.5 years of Cassini Plasma Spectrometer (CAPS) data to derive ion density, temperature, and flow velocity between 3 and $30 R_S$. However, their data set did not include any constraints on the field of view of the instrument so only a rough estimate of the structure of the plasma disk could be made. They concluded that a R^{-4} dependence describes the largest densities measured between 6 and $18 R_S$ fairly well. Persoon et al. (2009) presented ion and electron distributions derived from upper hybrid resonance emission measurements from 50 Cassini orbits combined with ion anisotropy and electron temperature measurements from the CAPS instrument. They used a diffusive equilibrium model to derive an L shell dependence of the water group ion density of $L^{-4.3}$ and of the hydrogen ions of $L^{-3.2}$, beyond $L = 5$.

Holmberg et al. (2012) presented Cassini LP ion density and azimuthal velocity for orbit 3 (1 February 2005) to 133 (27 June 2010). They presented a new LP analysis method making years of LP ion measurements available and also laying the foundation for LP analysis methods of future missions that includes LPs, for example, the Jupiter Icy Moons Explorer mission. This article builds on the study presented in Holmberg et al. (2012), using an improved analysis method and including measurements from 104 more orbits (about 6 more years) which provides a better statistical foundation and also the opportunity to study seasonal and solar cycle effects.

Section 2 gives a short introduction to the Cassini RPWS/LP measurements and data reduction method. The observation results are shown and discussed in section 3, and our conclusions are presented in section 4.

2. RPWS LP Data Reduction Method

The RPWS instruments are described by Gurnett et al. (2004). Detailed descriptions of the LP measurement method are provided by Gustafsson and Wahlund (2010), Morooka et al. (2011), and Holmberg et al. (2012).

The Cassini LP consists of a conducting titanium sphere, 5 cm in diameter, with a titanium nitride coating. The sphere is mounted on a boom, which gives the sphere a distance of 1.5 m to the nearest spacecraft surface. The LP measurements, used for this study, are performed by making voltage sweeps between -32 and $+32$ V (± 4 V is used for selected flybys). The probe attracts or repels plasma particles and charged dust according to its potential, that is, a current is generated. Each voltage sweep gives 512 data points that are fitted to a current-voltage curve. This study is focused on the ion current, for negative bias voltages, which for low voltages (< -5 V) shows a linear behavior. This limit is used since below -5 V the exponentially decreasing electron current, from energetic electrons that are able to reach the probe despite the negative bias voltage, is negligible. The linear fit to a sweep gives the slope b and the intercept value m .

In the outer magnetosphere the measured ion current is negligible, due to the very low ion density, and the LP is mainly measuring the photoelectron current I_{ph} , which is the current of electrons emitted from the probe due to the absorption of photons. The m values recorded in these regions show a spacecraft attitude dependence. This attitude dependence has previously been suggested to be due to a leakage current from the outer part of the boom that the probe is mounted to (Jacobsen et al., 2008). In Holmberg et al. (2012) this was corrected for by deriving one correction coefficient, for each spacecraft axis, which is used to correct the whole data set. However, the magnitude of the measured I_{ph} is due to the EUV radiation from the Sun, which is varying with the solar cycle. This means that in the attitude dependence there is also a time dependency that is not accounted for when using the attitude correction from Holmberg et al. (2012). A more accurate attitude correction, which includes the time variation, is used for the data set presented in this article.

To obtain all the time intervals when the dominant current contributor is I_{ph} , we select all data points that are (1) located outside of $9 R_S$, (2) not in eclipse of Saturn, (3) outside of any targeted flyby, and (4) outside of crossings of the plasma sheet. Plotting the chosen subsets against the spacecraft attitude shows a strong dependence on the angle between the probe and the Sun (as was reported in Holmberg et al., 2012; see their Figure A1). A correction coefficient for each outer magnetosphere measurement subset (that is required to be larger than 450 data points) is derived and compared to its neighboring coefficients. If the difference is larger than a chosen extreme value (0.11 nA), the outlier is removed. The two main causes of the outliers are (1) flapping of the magnetodisc and (2) measurements in the spacecraft wake.

The first cause of erroneous attitude correction coefficients is a periodic motion of the magnetodisc. Saturn's magnetosphere is known to exhibit magnetospheric periodicities in a number of properties, such as radio

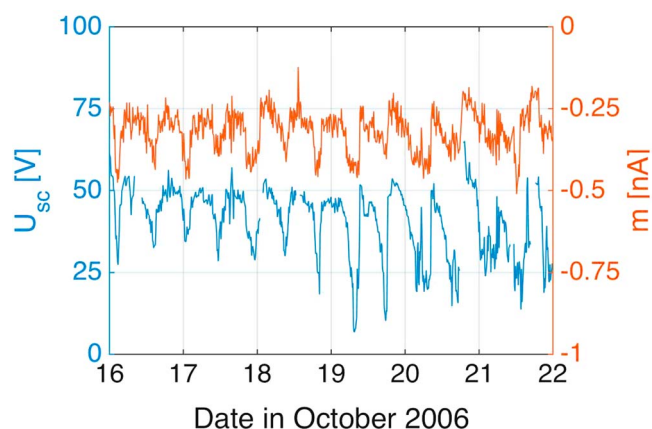


Figure 1. Cassini spacecraft potential U_{sc} (blue) and LP m value (red) for 16–22 October 2006. During this time interval the spacecraft moves within the radial distance 29 to 35 R_S . The flapping of the magnetodisc can be seen as drops in both U_{sc} and m with a periodicity close to the rotation rate of the planet, ~ 10.8 h.

emissions, plasma parameters, magnetic fields, and energetic neutral atoms (ENAs). The modulations all display a period close to the rotation rate of the planet. This periodic behavior is also clearly seen in the plasma density in the nightside of the middle and outer magnetosphere of Saturn (Khurana et al., 2009; Morooka et al., 2009). The modulation has been suggested to be due to a periodical motion of the plasma sheet in the Z direction, referred to as a flapping motion (Jia & Kivelson, 2012; Khurana et al., 2009; Morooka et al., 2009). In the outer magnetosphere and for the negative bias potential, the LP will not directly measure the varying plasma density since the measured I_{ph} is dominating and the contributing plasma current is too low. However, the currents collected and emitted by the much larger spacecraft body are also affecting the LP through the changing spacecraft potential U_{sc} . The changing U_{sc} will affect the amount of photoelectrons that are able to escape from the LP and the LP will measure a periodic I_{ph} modulation that is not correlated with the spacecraft attitude but with the rotation of Saturn. An example is shown in Figure 1, which shows the U_{sc} and m , recorded during a few days in October 2006, varying with a periodicity close to the rotation period of Saturn. The U_{sc} is obtained from the LP voltage sweeps. The spacecraft potential is easily detected in

the derivative of a sweep as the shift in voltage from 0 V, for an example see Gustafsson and Wahlund (2010) (their Figure 1c). The modulation due to the flapping of the magnetodisc is an actually periodic motion found in the Saturnian magnetosphere, and the LP measurements should not be corrected for this modulation. However, at a few time intervals the modulation period coincides with the changing attitude and this will create an erroneous attitude correction coefficient. The erroneous coefficients are removed as described in the previous paragraph.

The second cause of erroneous attitude correction coefficients is measurements performed in the spacecraft wake. Since the spacecraft acts as an obstacle in the plasma flow a wake will be formed behind the spacecraft, in relation to the plasma flow direction relative to the spacecraft; for an illustration see, for example, Engwall et al. (2009) or Miloch et al. (2012). The configuration of the wake will differ for different plasma conditions. However, based on the measured drop in the ion density related to the orientation of the LP, the majority of the spacecraft wake measurements can be excluded by removing measurements performed within 45° of the relative plasma flow direction. An example is shown in Figure 2; the drop in the ion density (red dots) can clearly be seen as the probe moves into the spacecraft wake. All measurements from within 45° of the relative plasma flow direction are excluded from the data set presented in this article.

After excluding the erroneous data points the attitude correction coefficients are estimated and interpolated to cover all LP measurement times. The interpolated correction coefficients are then used to correct the whole data set for the detected attitude dependence.

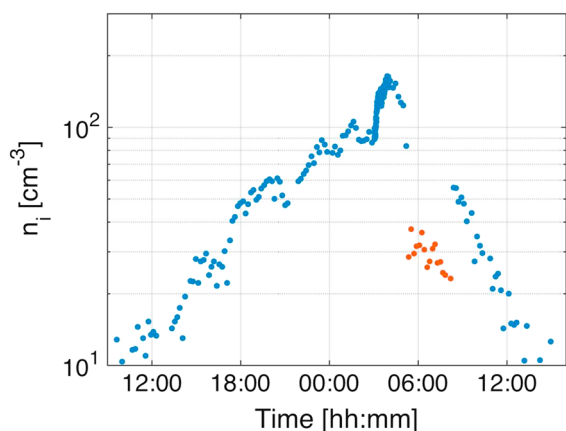


Figure 2. Cassini LP ion density measured between 16 February 2005, 9:00 and 17 February 2005, 16:00. The red dots show n_i measured in the spacecraft wake, where the angle between the LP and the relative plasma flow direction is less than 45° .

The second step in the LP ion density derivation method is to estimate the measured photoelectron current. For this analysis step Holmberg et al. (2012) used $F_{10.7}$ measurements as a proxy for solar EUV irradiance. $F_{10.7}$ has historically been used as a proxy for the solar EUV irradiance despite that it is well known that the two are not directly proportional to each other. The limitation of using the $F_{10.7}$ proxy has also been shown and discussed in a number of studies (e.g., Chen et al., 2011; Girazian & Withers, 2013). To improve our data reduction method, we have therefore replaced the $F_{10.7}$ proxy with the measured solar EUV irradiance, from the Thermosphere Ionosphere Mesosphere Energetics and Dynamics (TIMED) Solar EUV Experiment (SEE) and the Solar Stellar Irradiance Comparison Experiment (SOLSTICE) on the Solar Radiation and Climate Experiment (SORCE) spacecraft. The TIMED/SEE measurements provide irradiance for each wavelength, in 1 nm steps, from 0.5 to 190.5 nm at 1 AU. For this study the daily averaged level 3 data output is used. To avoid a known degradation problem of the TIMED/SEE instrument affecting the data for longer wavelengths, only wavelengths below 115 nm are used. Longer wavelengths are instead provided by SORCE/SOLSTICE that is measuring daily

solar UV flux (for 115 to 320 nm) in 1 nm steps at 1 AU. The solar EUV flux measurements are then propagated to Saturn using the tools provided at <http://lasp.colorado.edu/lisird/tools.html> (5 April 2017), which corrects for distance, phase, and a 27 day solar rotation. For an estimate of the EUV flux we use the integrated irradiance value from 1 to 160 nm as an EUV index, F_{EUV} . The choice to only use wavelengths shorter than 160 nm is motivated by studies of the photoelectric yield function for metals similar to TiN (e.g., Brace et al., 1988; Cairns & Samson, 1966). Brace et al. (1988) estimated the photoelectric yield for the Pioneer Venus Langmuir probe and showed that only 3% of the photoelectron emission is due to wavelengths longer than Lyman α (121.6 nm). Thus, a limit of 160 nm was chosen in order not to overestimate the contribution from longer wavelengths in generating the I_{ph} .

A linear relation between the measured I_{ph} and the measured F_{EUV} is assumed and used to derive the I_{ph} for all LP measurements. The magnitude of the measured I_{ph} shows a significant difference between the time intervals before and after August 2008. Before 2008 the average magnitude of I_{ph} is 0.38 nA; after August 2008 the average magnitude have changed to 0.25 nA. Median values give the same difference. This change in the measured I_{ph} is suspected to be due to the large amount of time that Cassini spent in the radiation belt of Saturn during 2008, which caused a degradation of the RPWS/LP electronics and/or altered the surface properties of the LP and therefore also the magnitude of the I_{ph} . For the time period before August 2008

$$I_{\text{ph},1} = -0.0050F_{\text{EUV},1} + 0.18, \quad (1)$$

and after August 2008

$$I_{\text{ph},2} = -0.0040F_{\text{EUV},2} + 0.19, \quad (2)$$

where $F_{\text{EUV},1}$ and $F_{\text{EUV},2}$ are the integrated EUV fluxes measured by TIMED/SEE and SORCE/SOLSTICE before and after August 2008, respectively. $F_{\text{EUV},1}$ and $F_{\text{EUV},2}$ range from around 130 to 200 $\mu\text{W}/\text{m}^2$.

Each voltage sweep performed by the LP is described by a slope b and intercept value m obtained from a linear fit to the measured current. The m and b values depend on the sum of all the different currents to the probe. For the region studied in this paper the two dominant currents are the ion current I_i of singly charged positive ions and the I_{ph} . For the short time duration of a sweep and for negative bias voltage the I_{ph} will be saturated to a constant value, since all photoelectrons will be able to leave the probe. This gives that $m = I_{\text{ph}} + a$, where a is the intercept value of I_i . Fahleson (1967) provided a numerically convenient approximation for the I_i to the probe, as

$$I_i \approx I_{i0} \left(1 - \frac{q_i (U_1 + U_{\text{bias}})}{\frac{m_i v_i^2}{2} + k_B T_i} \right), \quad (3)$$

where

$$I_{i0} \approx -A_{\text{LP}} n_i q_i \sqrt{\frac{v_i^2}{16} + \frac{k_B T_i}{2\pi m_i}}. \quad (4)$$

U_1 is the spacecraft potential measured at the probe, U_{bias} is the bias potential of the probe, k_B is the Boltzmann constant, $q_i/T_i/n_i/v_i/m_i$ are the charge/temperature/density/drift velocity/mass of the i th ion species, and A_{LP} is the surface area of the Langmuir probe. Relating the derived m and b values to the theoretical description of the current given by Fahleson (1967) results in

$$I_i + I_{\text{ph}} = m + bU_{\text{bias}}, \quad (5)$$

where

$$m \approx I_{i0} \left(1 - \frac{q_i U_1}{\frac{m_i v_i^2}{2} + k_B T_i} \right) + I_{\text{ph}}, \quad (6)$$

and

$$b \approx -\frac{I_{i0} q_i}{\frac{m_i v_i^2}{2} + k_B T_i}. \quad (7)$$

Equations (6) and (7) give

$$I_{i0} \approx m - I_{\text{ph}} - bU_0 \approx a - bU_0, \quad (8)$$

where U_0 is the potential value for $l = 0$ that is used as a proxy for U_1 . Investigating the term bU_0 shows that for 90% (96%) of the whole data set the term bU_0 is smaller than 5% (10%) of the $a = m - l_{ph}$ value. Since $bU_0 \ll a$, this term has been omitted from the presented derivation of the ion density. Assuming that the thermal component of the ion motion is small and using equations (4) and (7) we derive

$$-l_{i0}b \approx \left(-A_{LP}n_iq_i \sqrt{\frac{v_i^2}{16}} \right)^2 \left(\frac{q_i}{m_i v_i^2} \right) = (A_{LP}n_iq_i)^2 \left(\frac{q_i}{8m_i} \right) \Rightarrow, \quad (9)$$

$$n_i \approx \frac{1}{A_{LP}q_i} \sqrt{\frac{-8m_i l_{i0}b}{q_i}}, \quad (10)$$

which is used to obtain the ion density n_i from the LP measurements. The effect on the estimation of the azimuthal ion velocity from omitting the thermal component is discussed in Holmberg et al. (2012). It is difficult to estimate how large the effect on the LP n_i is, but the good agreement between the LP n_i and the n_e derived from upper hybrid resonance frequency f_{UHR} measurements, see Figure 4, is a strong indicator that the effect is small.

The LP measurements are also affected by a secondary electron current I_{se} produced by 250 to 450 eV electrons located between 6 and 10 R_S , which has been studied in detail by Garnier et al. (2012, 2013, 2014). A significant I_{se} is detected in the sweep as altering the slope b from positive to negative (Garnier et al., 2013; Holmberg et al., 2012). For this reason, no sweep data with $b < 0$ are included in this study.

The final step in deriving the LP n_i includes estimating an effective ion mass m_i . The method to estimate m_i is described in detail in Holmberg et al. (2012) Appendix C. The earlier estimate of m_i , by Holmberg et al. (2012), included the use of the W^+ and H^+ scale heights derived from the CAPS data by Thomsen et al. (2010) given for 6.5 to 16.5 R_S . For the data presented in this article we replace these estimates with scale heights derived from the f_{UHR} measurements presented by Persoon et al. (2009), who provides scale heights also within 6.5 R_S . How to derive electron density from f_{UHR} is explained by Gurnett et al. (2005).

3. Results and Discussion

3.1. Structure of the Plasma Disk

With the above described corrections to the analysis method presented in Holmberg et al. (2012), we derive ion densities of the inner plasma disk of Saturn. The equatorial n_i , limited to $R < 12 R_S$ and $|z| < 0.5 R_S$, is presented in Figures 3 and 4. The limitation $|z| < 0.5 R_S$ is used since this is the region where the water group ions are the dominant ion species (Holmberg et al., 2012). No data from the second half of 2013 and from 2014 are included in the analysis, due to the limited configuration of the Cassini orbit. At this time interval the apoapsis of the orbit was located farther away than 12 R_S or above/below 0.5 R_S of the equator plane. Due to the better coverage of the data set used in this study, Figure 3 shows a more continuous plasma disk than what was presented in Holmberg et al. (2012). Direct plume passages of the Enceladus's plume are clearly visible as the density peak located at the orbit of Enceladus, at around 3.95 R_S . Equally distinct density increases cannot be seen at the orbits of any of the other moons.

The median density for each 0.1 R_S radial bin is calculated and fitted to

$$n_{i,eq} = \frac{n_0}{\frac{1}{2} \left(\left(\frac{R_0}{R} \right)^c + \left(\frac{R}{R_0} \right)^d \right)}, \quad (11)$$

following the notation of Persoon et al. (2013). The fit gives a maximum density of $n_0 = 64.9 \text{ cm}^{-3}$ at $R_0 = 4.47 R_S$ with radial dependences $c = 6.66$ and $d = 3.79$ and is shown as the black line in Figure 3a. Fitting equation (11) to the density above 50 cm^{-3} , radial distance between 4.1 and 5.5 R_S , we obtain a density maximum of 70.7 cm^{-3} located at 4.59 R_S . The estimated density maximum and distance is in good agreement with the values of 72 cm^{-3} at 4.6 R_S estimated by Persoon et al. (2013). A study of n_i before and after Saturn equinox (11 August 2009) revealed no detectable effect in the radial distribution (not shown).

Figure 3b shows the number of data points, N_{bin} , for each 2.53 cm^{-3} density bin and 0.1 R_S radial bin. Figure 3c shows the probability, $P_{0,1}$, to measure a certain n_i for each 0.1 R_S bin. The relatively low values, around 30 cm^{-3} , usually measured at the orbit of Enceladus are a somewhat surprising result since Enceladus is the dominant

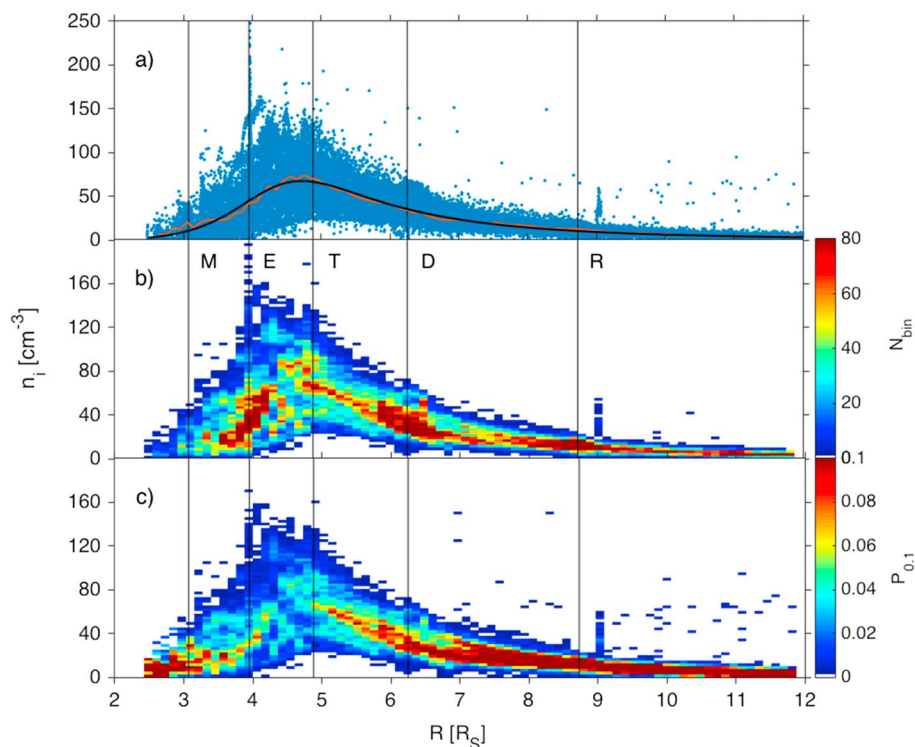


Figure 3. Equatorial ion densities derived from RPWS/LP recorded during the time interval 1 February 2005 (orbit 3) to 29 June 2016 (orbit 237). The density measurements are limited to $|z| < 0.5 R_S$ from the equator plane. The vertical black lines give the positions of the moons Mimas ($\sim 3.07 R_S$), Enceladus ($\sim 3.95 R_S$), Tethys ($\sim 4.88 R_S$), Dione ($\sim 6.25 R_S$), and Rhea ($\sim 8.73 R_S$). (a) Individual data points (blue dots), the median value for each $0.1 R_S$ radial bin (red line), and the fit to the median values given by equation (11) (black line), using $n_0 = 64.9 \text{ cm}^{-3}$, $R_0 = 4.47 R_S$, $c = 6.66$, and $d = 3.79$. (b) The radial region and density interval has been divided into small bins ($0.1 R_S$ and 2.53 cm^{-3} , i.e., 100 bins between 0 and 250 cm^{-3}), and the number of points in each bin is given by the color. (c) The probability to measure a certain ion density for each $0.1 R_S$ radial bin.

neutral source. This is likely due to hot electron impact ionization being an important source process in this region, which is further discussed in section 3.2.

An unusual feature shown in Figure 3 is the small density peak of up to 60 cm^{-3} located around $9 R_S$, which consists of about 15 data points recorded during 6 min on 11 January 2011. The feature can also be seen in the Cassini Plasma Spectrometer (CAPS) measurements (not shown) as an increase in hot electrons ($>100 \text{ eV}$) and hot ions ($>1 \text{ keV}$) and a depletion of cold ions and electrons. These are common characteristics of interchange injection events. It has been shown that the main outward transport process in Saturn's middle magnetosphere is driven by the rapid rotation of the magnetosphere that creates a strong centrifugal force (e.g., André et al., 2005; Burch et al., 2005; Hill et al., 2005). Due to this process, cool and dense plasma originating in the inner magnetosphere is driven outward and replaced through interchange injection events by hotter and less dense plasma from the outer magnetosphere; for a review see Thomsen (2013). An injection of hot electrons would increase the emission of secondary electrons from the LP which in turn would be detected as an increase in density. In this way the LP may also be used to detect interchange injection events. However, the LP injection measurements commonly involve only one or two measurement points for each event, which can be seen as the few data points found throughout the plasma disk with density values several times the median ion density. The LP commonly performs one voltage sweep every 10 min, but for targeted flybys a frequency of 24 s is used instead. The higher measurement frequency was used during the time period when the unusual density peak around $9 R_S$ was recorded, since a flyby of the moon Rhea was performed about 30 min before the event. This resulted in more measurements being performed within the injection event, and the apparent density peak became more prominent. The feature can also be detected in the frequency-time spectrogram from the RPWS electric antennas (not shown) as a strong increase in the wave emissions between 6 and 20 kHz. These emissions appear to be higher-order multiharmonic electron cyclotron waves inside the interchanging flux tube (Menietti et al., 2008).

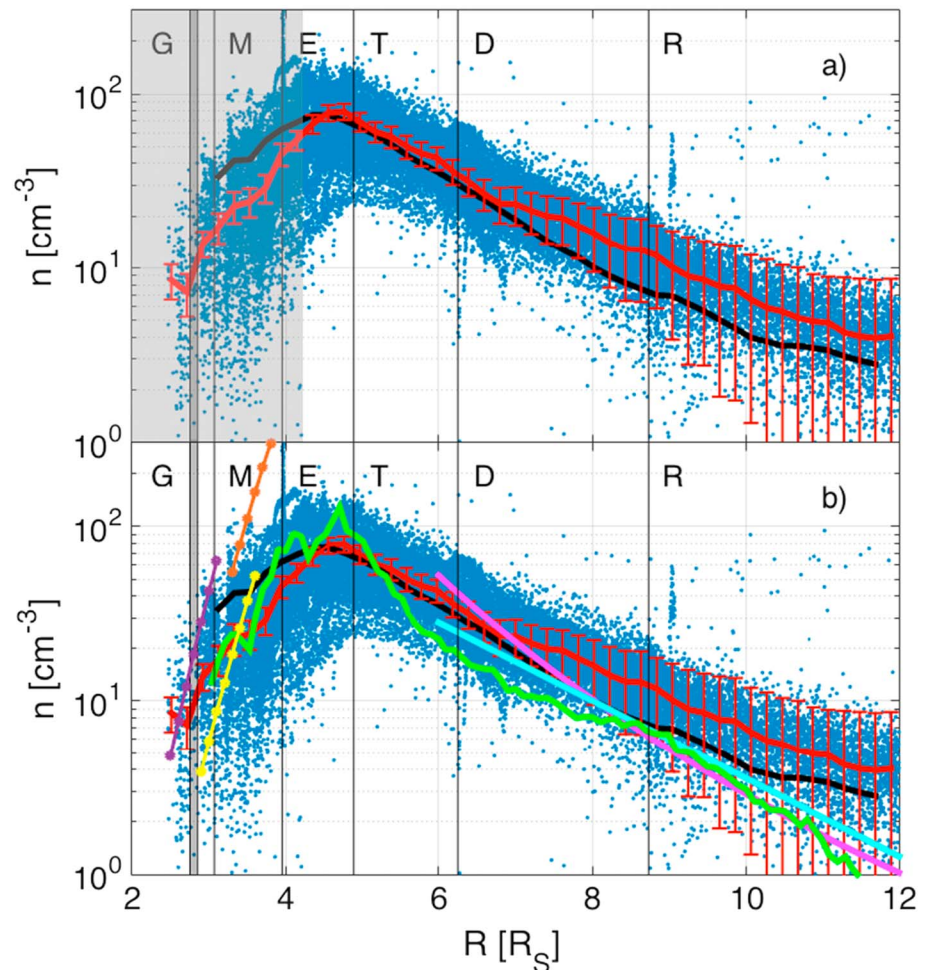


Figure 4. (a) Equatorial, $|z| < 0.25 R_S$, ion densities (blue dots) derived from RPWS/LP as a function of radial distance from Saturn. The median value (red line) and the median error (red error bars) for each $0.2 R_S$ radial bin is included. The black line shows the fit to the equatorial, $|z| < 0.25 R_S$, n_e derived from the f_{UHR} . The vertical black and gray lines give the positions of the G ring and the moons Mimas, Enceladus, Tethys, Dione, and Rhea. The gray rectangle marks the region, $< 4.2 R_S$, where n_e and LP n_i differs, which might be due to an underestimation of the LP n_i . (b) CAPS ion density measurements from three different studies: the exponential (cyan) and power law (magenta) fit of the CAPS ion density measured within $\pm 5^\circ$ of the equatorial plane and outside of $6 R_S$ (Thomsen et al., 2010), the obtained ion density (green) measured within $\pm 10^\circ$ magnetic latitude and between 3 and $12 R_S$ (Livi et al., 2014), and the CAPS ion densities for the years 2007 (purple line with circular markers), 2010 (yellow line with circular markers), and 2012 (orange line with circular markers) measured within $\pm 5,000$ km ($\sim 0.083 R_S$) in z and between 2.4 and $3.8 R_S$ (Elrod et al., 2014).

Figure 4 shows the derived ion density (blue dots) in logarithmic scale. Figure 4 shows that the density variation is large, also shown by, for example, Holmberg et al. (2012), more than 1 order of magnitude for the innermost part of the plasma disk and decreasing outward. This has been suggested to be due to a seasonal variation of the neutral and ion production in the main rings, which will be discussed further in section 3.3. Figure 4 also includes the estimated error of the obtained median density. The error is based on the estimated standard errors of the slope b and intercept value m , defined in section 2, using linear regression theory. The error of the obtained n_i for each voltage sweep, is then estimated by propagating the errors of b and m . Finally, the median density for each $0.2 R_S$ radial bin is calculated (red line of Figure 4) and the median error for each bin is given as a red error bar. No significant difference is seen when using the average ion density instead of the median values, if excluding all measurements recorded in the close vicinity of Enceladus.

Figure 4 also shows the estimated median electron density n_e , black lines in Figures 4a and 4b, obtained from upper hybrid resonance frequency f_{UHR} measurements from the RPWS electric field antennas. When the f_{UHR} is easily detected and not disturbed by other frequencies located in the same frequency range, it is an accurate

method for density measurements. The good agreement between the obtained LP ion density and the electron density derived from the f_{UHR} , usually within 3 cm^{-3} with a maximum difference of 6 cm^{-3} outside of $4.2 R_S$, is a confirmation of the good accuracy of both measurement techniques. The notation n_e will further on always refer to the electron density derived from the f_{UHR} measurements.

Figure 4b includes CAPS ion density measurements from three different studies: the exponential (cyan) and power law (magenta) fit of the CAPS ion density measured within $\pm 5^\circ$ of the equatorial plane and outside of $6 R_S$ (Thomsen et al., 2010), the obtained ion density (green) measured within $\pm 10^\circ$ magnetic latitude and between 3 and $12 R_S$ (Livi et al., 2014), and the CAPS ion densities for the years 2007 (purple line with circular markers), 2010 (yellow line with circular markers), and 2012 (orange line with circular markers) measured within $\pm 5,000 \text{ km}$ ($\sim 0.083 R_S$) in Z and between 2.4 and $3.8 R_S$ (Elrod et al., 2014). A detailed description of the CAPS instrument is given by Young et al. (2004). The comparison between the different data sets presented in Figure 4b: the median LP n_i (red), the RPWS n_e (black), the CAPS n_i from Thomsen et al. (2010) (cyan and magenta), and the CAPS n_i from Livi et al. (2014) (green) is accurate despite the different conditions used to define the equatorial plane. This is because most of the data are anyhow limited to within $\pm 0.2 R_S$ due to Cassini's orbit configurations. Hence, the choice of $\pm 0.25 R_S$, $\pm 5^\circ$, or $\pm 10^\circ$ has a negligible effect on the estimated median n_e and n_i .

Within $4.2 R_S$ the n_e and LP n_i start to deviate; this region is emphasized with a gray area in Figure 4a. The disagreement is suspected to be due to the larger amount of cluster ions that are present in the inner magnetosphere. Cluster ions would change the value of the effective ion mass m_i , which could cause the ion density in the inner region to be underestimated. However, it is interesting to see that the CAPS ion densities presented by Livi et al. (2014) agree well with the LP n_i measurements. This might imply that the CAPS instrument also is affected by the presence of the cluster ions. But the CAPS measurements should be used with great caution within 4 to $6 R_S$, since a significant amount of penetrating background radiation contaminates the CAPS measurements and complicates the data analysis in this region (e.g., Elrod et al., 2012; Livi et al., 2014; Young et al., 2004).

3.2. Shifted Plasma Disk Density Peak

One interesting feature of the plasma structure in the inner magnetosphere of Saturn is the shifted plasma disk density peak. The plasma disk is created from ionization and charge exchange of the material expelled from the moon Enceladus, and it would therefore be easy to conclude that the maximum density of the plasma disk should be located at the neutral source location, that is, at the orbit of Enceladus. However, the median plasma density peak is not located at the orbit of Enceladus, at $3.95 R_S$, but at $4.6 R_S$, as shown in Figures 3 and 4. The shifted location of the density peak is clearly visible in all three data sets: the LP n_i (red), the RPWS n_e (black), and the CAPS n_i (green).

The shifted plasma density peak can be explained by hot electron impact ionization that is an important ionization process in this region. The hot electron component originates from the middle and outer magnetosphere and is transported inward by interchange like injection events, as discussed in section 3.1. The peak of the hot electron density is located closer to $7 R_S$ since the hot plasma subsequently gradient and curvature drifts out of the injected flux tube, as suggested by Hill et al. (2005) and Rymer et al. (2008). As new ions are produced by hot electron impact ionization the largest ion production rate, in the region close to the equatorial plane, will be found in between the maxima of the neutral density and the hot electron density. It should be noted that the equatorial plasma density peak does not correspond to the peak of the total flux tube content, which instead peaks around magnetic L shell 6.3 (Sittler Jr et al., 2008) and 6.6 (Holmberg et al., 2016).

To illustrate the idea, consider one important ionization process in the inner plasma disk, for example, $\text{H}_2\text{O} + e_h \rightarrow \text{H}_2\text{O}^+ + 2e$. The corresponding water ion production rate $P_{\text{H}_2\text{O}^+} = n_{\text{H}_2\text{O}} n_{e_h} \alpha$, where $n_{\text{H}_2\text{O}}$ is the H_2O density, n_{e_h} is the hot electron density, and α is the reaction rate coefficient. For n_{e_h} we use the electron density above 12.6 eV, the ionization threshold for water, measured during orbit 4, 5, 119, and 122 by the CAPS ELS instrument. For a detailed description of the numerical computation of the plasma moments obtained from CAPS ELS measurements see Lewis et al. (2008). The average n_{e_h} for each $0.1 R_S$ radial bin is shown in Figure 5 (blue line). The best fit using equation (11) for the hot electrons, with $n_0 = 1.15 \text{ cm}^{-3}$, $R_0 = 6.85 R_S$, $c = 6.99$, and $d = 4.92$, is shown as the black line. The fit is used to derive $P_{\text{H}_2\text{O}^+}$ since penetrating radiation contaminates the CAPS ELS sensor within 4 to $6 R_S$, which limits the availability of measurements in this region (e.g., Elrod et al., 2012). The electron density presented in Figure 5 may be compared to the hot electron densities presented by Schippers et al. (2008) and Sittler et al. (1983). Schippers et al. (2008) derived hot

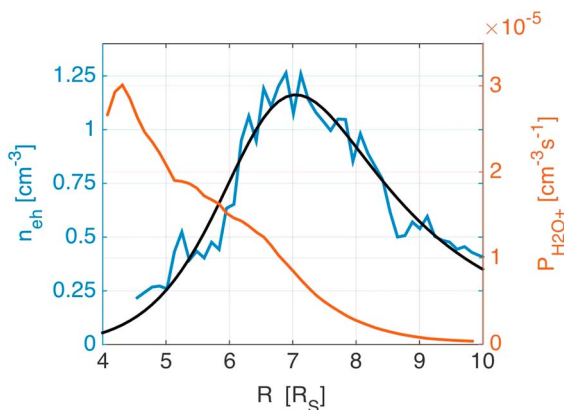


Figure 5. Average equatorial hot (> 12.6 eV) electron density n_{eh} (blue) measured by CAPS ELS for orbit 4, 5, 119, and 122. Fit to average n_{eh} (black), using equation (11) with $n_0 = 1.15 \text{ cm}^{-3}$, $R_0 = 6.85 R_S$, $c = 6.99$, and $d = 4.92$. The H_2O^+ production rate $P_{\text{H}_2\text{O}^+}$ (red) due to impact ionization between hot electrons and H_2O shows a production peak close to $4.3 R_S$.

electron densities (100 eV to 10 keV) for orbit 24, giving densities between 0.01 cm^{-3} to 0.2 cm^{-3} between 5 and $12 R_S$. Sittler et al. (1983) presented Voyager 1 Plasma Subsystem (PLS) electron densities (for energy range 10 eV to 5.95 keV) between 5 and 15 cm^{-3} , before correcting for the spacecraft potential, between 5.2 and $7.3 R_S$, which is the radial range when the spacecraft was within $\pm 0.5 R_S$ during the flyby on 13 November 1980. Correcting for the spacecraft potential gives an estimated total electron density of around 25 cm^{-3} at the ring plane crossing; see their Figure 13. The above studies confirm that the density presented in Figure 5 is in the accurate range since the density (and energy range) falls within the ranges presented by Schippers et al. (2008) and Sittler et al. (1983).

Using $P_{\text{H}_2\text{O}^+} = n_{\text{H}_2\text{O}} n_{eh} \alpha$, with $n_{\text{H}_2\text{O}}$ from Fleshman et al. (2013) (their Figure 1), n_{eh} presented in Figure 5, and the reaction rate coefficient $\alpha = 9.1 \times 10^{-8} \text{ cm}^3 \text{ s}^{-1}$ derived for $T_{eh} = 160 \text{ eV}$ by Fleshman et al. (2010) from measurements by Orient and Strivastava (1987), we estimate $P_{\text{H}_2\text{O}^+}$ shown in Figure 5 (red line). The $P_{\text{H}_2\text{O}^+}$ peak is located at $4.3 R_S$, which shows how the distribution of the hot electrons can affect the location of the ion density production peak. A more accurate study of the plasma disk

structure would have to include all dominant chemical processes. Such a study has already been performed and presented by Fleshman et al. (2013) who, among many other results, estimated the equatorial ion density of the inner plasma disk. Fleshman et al. (2013) derived a plasma density peak located between 4.2 and $4.5 R_S$, see their Figure 2, but did not include any discussion about this result. A more detailed study should also take into account that the reaction rate coefficient α is temperature dependent. However, this does not change the conclusion that the density distribution of hot electrons can shift the plasma disk away from the main neutral source region, so for simplicity we chose to use a constant reaction rate coefficient.

3.3. Solar Cycle and Seasonal Modulations

Another interesting feature of the inner magnetosphere of Saturn is the seasonal variation found in the plasma between the main rings and Enceladus (Elrod et al., 2012, 2014; Persoon et al., 2015). The seasonal variation was first predicted by Tseng et al. (2010), who used a Monte Carlo test particle model to simulate ion and neutral motion within $2.5 R_S$. Assuming that photodissociation of ring ice particles is the main source of O_2 and, subsequently, O_2^+ in this region, the O_2 and O_2^+ production rate will vary with the varying insolation angle. A large insolation angle, maximum $\sim 27^\circ$ at winter and summer solstice, will result in a larger O_2 and O_2^+ production rate and vice versa. As the particles are transported outward, due to collisional interactions, a seasonal variation could also be expected in the particle densities in between the main rings and Enceladus. A seasonal variation was also found in the CAPS n_i (Elrod et al., 2012, 2014) and the RPWS n_e (Persoon et al., 2015).

With the 11 years RPWS/LP data set we can now extend the results of these studies and also investigate the solar cycle modulation of Saturn's inner plasma disk.

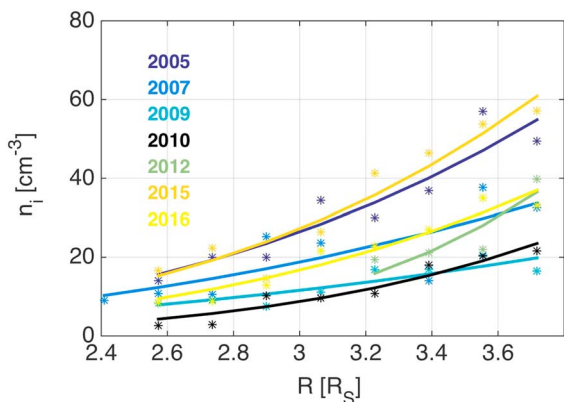


Figure 6. Equatorial, $|z| < 0.25 R_S$, median ion densities from 2005 to 2016 in between 2.4 and $3.8 R_S$. Each marker corresponds to the median ion density \bar{n}_i for each $0.16 R_S$ radial bin. The color coded lines give the fit, $n_i = aR^k$, to the median values for each year. The values of a and k are listed in Table 1.

The LP n_i measurements recorded between 2.4 and $3.8 R_S$ are separated by year, and the median value (and fit to the median values) for each 0.16 radial bin is shown in Figure 6. A clear yearly variation is shown; the trend is lower densities closer to equinox (August 2009) and solar minimum (mid-2008 to early 2010). Since equinox and solar minimum occurred within such a close time span it is difficult to separate the importance of the two modulations. However, the low densities measured in 2016, when the insolation angle was larger than in 2015 but the solar EUV flux was smaller, imply that the changing solar cycle is also an important contributing factor in the detected density modulation. This is better illustrated in Figure 7, which shows the median ion density at $3.7 R_S$ and the insolation angle θ_{SR} versus year. The density variation $\Delta \bar{n}_i \approx 40 \text{ cm}^{-3}$ compares well with the varying average electron density, $\Delta \bar{n}_e \approx 35 \text{ cm}^{-3}$ at $4 \pm 0.25 R_S$ and 50 cm^{-3} at $3.5 \pm 0.25 R_S$, presented by Persoon et al. (2015). The ion density variation is in good agreement with the changing insolation angle, except for the year 2016.

Table 1

R Dependence of Yearly Median Ion Density (From 0.16 R_S Radial Bins), Given by n_i = aR^k, for 2.4 < R < 3.8 R_S

Parameter	2005	2007	2009	2010	2012	2015	2016
a (cm ⁻³)	0.62 ± 0.22	0.93 ± 0.75	0.74 ± 0.34	0.05 ± 0.04	0.02 ± 0.01	0.44 ± 0.23	0.29 ± 0.10
k	3.41 ± 0.34	2.73 ± 0.77	2.50 ± 0.44	4.62 ± 0.68	5.88 ± 0.49	3.76 ± 0.51	3.70 ± 0.33

Note. The parameters are given with 95% confidence intervals.

Plotting the median equatorial ion density at 3.7 R_S against the solar EUV flux, integrated over wavelengths 0.5 to 98.5 nm, shows a better agreement. Figure 8 shows the F_{EUV} measured by TIMED/SEE (blue line), as described in section 2, the median equatorial ion density \tilde{n}_i (red dots) by year, and the average electron density \tilde{n}_e (black dots) for each 6 months time interval, for 3.7 R_S (upper panel) and 5 R_S (lower panel). The upper wavelength limit of 98.5 nm is used since the ionization threshold for H₂O is 98.4 nm (Huebner et al., 1992). The plasma density, from both data sets, clearly follows the varying EUV flux and the trend can also be seen at 5 R_S but farther out the trend is less significant, most likely due to the increasing importance of hot electron impact ionization.

The strong correlation between the F_{EUV} and the plasma density is somewhat surprising since earlier studies have suggested that a varying photoionization rate due to the changing solar EUV flux alone could not result in such large variations as the one seen in Figures 7 and 8, (e.g., Elrod et al., 2014). To estimate the change in density due to the changing solar EUV flux, we derive the photoionization rate coefficients κ_j , where $j = 1, 2, 3, 4$, corresponding to (1) the larger flux at date 30 June 2005, (2) the smaller flux at 30 June 2009, (3) larger flux at 30 June 2015, and (4) smaller flux at 30 June 2016. The change in plasma density over time is given by the continuity equation $dn/dt = Q - L$, where Q includes all source and L all loss processes. The dominant ionization processes are photoionization and hot electron impact ionization $Q = \kappa n_n + kn_{eh}n_n$, where κ is the photoionization rate coefficient, n_n is the neutral density, k is the impact rate coefficient, and n_{eh} is the hot electron density. The dominant loss processes are recombination and transport $L = \alpha_{eff}n_in_e + n/t$, where α_{eff} is an effective reaction rate coefficient and t is the radial transport time. Assuming quasineutrality of the plasma disk, that is, $n_i \approx n_e \approx n$, for the steady state situation we get $\kappa n_n + kn_{eh}n_n = \alpha_{eff}n^2 + n/t$. Holmberg et al. (2016) showed that the dominant loss process in the plasma disk is transport loss, so for a rough estimate we use $\kappa n_n + kn_{eh}n_n = n/t$.

The hot electron density has been suggested to be part of an electron circulation pattern where a fraction of the electrons of internal origin, which are transported to the outer magnetosphere, are being adiabatically heated when injected back into the inner and middle magnetosphere by interchange injections (Rymer et al., 2008). If the source of the hot electrons are the cold electrons in the inner magnetosphere, it is reasonable to assume that the hot electron density also will exhibit a EUV flux dependency. Since investigating the EUV dependence of hot electrons in Saturn's magnetosphere is beyond the scope of this article, we will instead just look at two cases: (a) assuming that n_{eh} follows the plasma density modulation like $n_{eh} = Cn_e$, where C is a constant, and (b) assuming that n_{eh} is independent of the F_{EUV} modulation.

For case (a) we obtain

$$n_j = \frac{t\kappa_j n_n}{1 - tkCn_n} \quad j = 1, 2, 3, 4, \quad (12)$$

where the subscripts 1 and 3 correspond to large F_{EUV} (at 30 June 2005 and 30 June 2015) and 2 and 4 to small F_{EUV} (at 30 June 2009 and 30 June 2016). Equation (12) gives $n_j/n_{j+1} = \kappa_j/\kappa_{j+1}$. For case (b) we obtain

$$n_j = t\kappa_j n_n + tkn_n n_{eh} \quad j = 1, 2, 3, 4, \quad (13)$$

which gives

$$\frac{n_j}{n_{j+1}} = \frac{\kappa_j + kn_{eh}}{\kappa_{j+1} + kn_{eh}}. \quad (14)$$

The photoionization rate coefficient is given by $\kappa = \int_{\lambda_1}^{\lambda_2} \sigma(\lambda)\Phi(\lambda)d\lambda$, where $\sigma(\lambda)$ is the photoionization cross section and $\Phi(\lambda)$ is the photon flux at wavelength λ (Huebner & Carpenter, 1979). The dominant

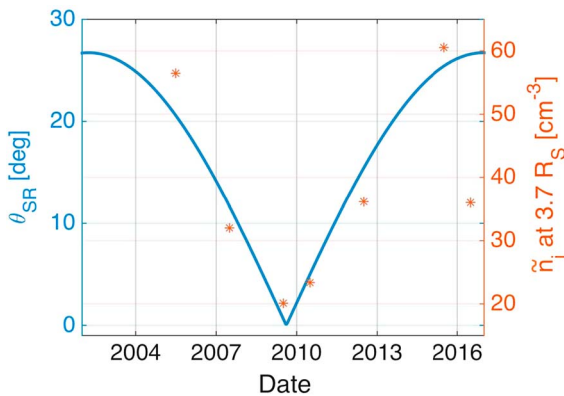


Figure 7. Median equatorial, $|z| < 0.25 R_S$, ion density at 3.7 R_S and the angle θ_{SR} between the ring plane and the Sun direction versus time from year 2002 to 2017. The date label marks 1 January for each year.

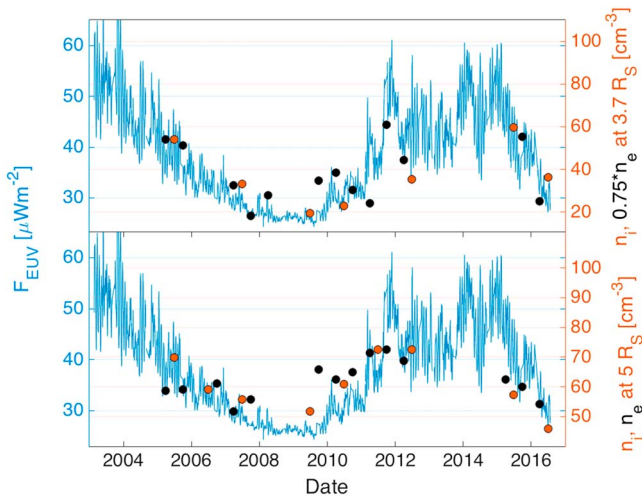


Figure 8. Integrated (0.5–98.5 nm) solar EUV flux, F_{EUV} , and median equatorial, $|z| < 0.25 R_S$, ion density (red dots) at (top) $3.7 R_S$ and (bottom) $5 R_S$ versus time from year 2003 to 2017. The average equatorial, $|z| < 0.25 R_S$, electron density derived from f_{UHR} measurements for 6 months time intervals is plotted as black dots. Figure 8 (top) shows $0.75 n_e$ to compensate for the difference between n_e and LP n_i for smaller radial distances, as discussed in section 3.1. The date label marks 1 January for each year.

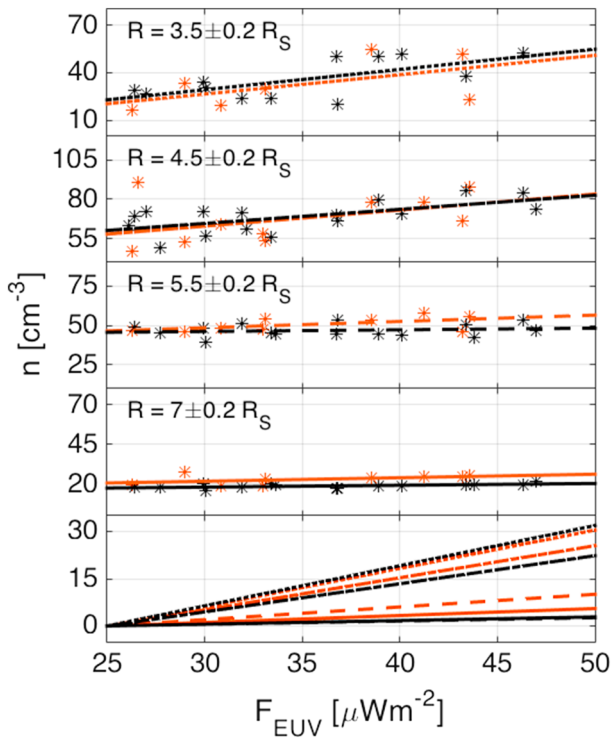


Figure 9. Yearly median ion density (red) and 6 months average electron density (black) at 3.5 ± 0.2 , 4.5 ± 0.2 , 5.5 ± 0.2 , and $7 \pm 0.2 R_S$ against solar EUV flux. (first to fourth panels) The $0.7 n_e$ to compensate for the difference between n_e and LP n_i for smaller radial distances, as discussed in section 3.1. The best fits are given by $n_i = A_i F_{EUV} + B_i$ and $n_e = A_e F_{EUV} + B_e$ where the values of A_i , B_i , A_e , and B_e are listed in Table 2. (fifth panel) The difference in density between low and high F_{EUV} for $3.5 \pm 0.2 R_S$ (dotted), $4.5 \pm 0.2 R_S$ (dash dotted), $5.5 \pm 0.2 R_S$ (dashed), and $7 \pm 0.2 R_S$ (solid).

neutrals in the equatorial plane of the plasma disk are O, OH, and H₂O. The photoionization cross sections $\sigma(\lambda)$ for O, OH, and H₂O are given at <http://www.phidrates.space.swri.edu> (15 February 2017) and based on the work presented in Huebner et al. (1992) and Huebner and Mukherjee (2015). The ionization thresholds for O, OH, and H₂O are 91.0, 92.8, and 98.4 nm, respectively (Huebner et al., 1992). We are therefore only interested in $\lambda < 98.5$ nm and use the EUV flux measurements performed by the TIMED/SEE instrument for 1 AU and propagated to the location of Saturn for the dates 30 July years 2005, 2009, 2015, and 2016. Using the method described above, the photoionization rate coefficients for each component and time are calculated. To estimate the effective photoionization rate coefficients, we use

$$\kappa_j = \frac{\kappa_O n_O + \kappa_{OH} n_{OH} + \kappa_{H_2O} n_{H_2O}}{n_O + n_{OH} + n_{H_2O}}, \quad (15)$$

where the neutral densities of O, OH, and H₂O from Fleshman et al. (2013) are used. Equation (11) gives $\kappa_1 \approx 6.13 \times 10^{-9} \text{ s}^{-1}$, $\kappa_2 \approx 4.70 \times 10^{-9} \text{ s}^{-1}$, $\kappa_3 \approx 5.41 \times 10^{-9} \text{ s}^{-1}$ and $\kappa_4 \approx 3.69 \times 10^{-9} \text{ s}^{-1}$.

For case (a), using κ_1 and κ_2 , $n_1/n_2 \approx 0.77$ which is equivalent to $\Delta n_i \approx 12 \text{ cm}^{-3}$ for $n_1 = 54 \text{ cm}^{-3}$. Equation (14) shows that, since $kn_{eh} > 0$, n_1/n_2 for case (b) will always be smaller than for case (a). The derived $\Delta n_i \approx 12 \text{ cm}^{-3}$ should be compared with the density drop shown in Figure 8 which for the LP n_i is around 34 cm^{-3} for the decrease from 2005 to 2009. This could indicate that the additional 22 cm^{-3} is due to the decrease in plasma density due to the decreasing insolation angle, that is, the seasonal variation.

For the density variation from year 2015 to 2016 the large insolation angle would indicate a large plasma density but instead a density decrease is measured. For case (a) we estimate $n_3/n_4 = \kappa_3/\kappa_4 \approx 0.68$ which is equivalent to $\Delta n_i \approx 20 \text{ cm}^{-3}$ for $n_3 = 60 \text{ cm}^{-3}$. This agrees well with the measured density drop of about 25 cm^{-3} shown in Figure 8 (top). However, the density in this region depends both on the F_{EUV} and the insolation angle, so a smaller density decrease than the one detected was expected since at this time period the F_{EUV} is small and the insolation angle large. This could indicate that an additional, unknown, EUV-dependent source process is also affecting the plasma density in the inner part of the plasma disk, since the measurements show a stronger dependence on F_{EUV} than what could be estimated.

It is interesting to note that Elrod et al. (2012) also included ion density measurements from the Voyager 2 Plasma Subsystem (PLS) in their seasonal modulation study. The PLS n_i does not correlate well with the changing seasons, since it shows a high density, around 110 cm^{-3} at $2.8 R_S$, despite being close to equinox. Simulated ion densities, using Voyager 2 data inputs, of around 100 cm^{-3} at $2.8 R_S$ was also presented by Lazarus and McNutt Jr. (1983). The PLS n_i correlates better with the EUV flux modulation presented in Figure 8 since the Voyager 2 ring plane crossing occurred close to the solar maximum in 1980. However, the Voyager 2 PLS data are from a single flyby, of a very dynamic region, and should therefore be considered with caution.

The plasma density dependence on F_{EUV} at four different radial distances, 3.5 , 4.5 , 5.5 , and $7 R_S$, are given by Figure 9. The yearly median n_i (red stars) and average, over 6 months intervals, n_e (black stars) are plotted against F_{EUV} , and the best fits are given by $n_i = A_i F_{EUV} + B_i$ (red lines) and $n_e = A_e F_{EUV} + B_e$ (black lines), with the coefficients given in Table 2.

Table 2

F_{EUV} Dependence of Yearly Median Ion Density and Average, Over 6 Months Intervals, Electron Density, Given as $n_i = A_i F_{EUV} + B_i$ and $n_e = A_e F_{EUV} + B_e$ for Radial Distances $3.5 \pm 0.2, 4.5 \pm 0.2, 5.5 \pm 0.2,$ and $7 \pm 0.2 R_S$

Parameter	$3.5 \pm 0.2 R_S$	$4.5 \pm 0.2 R_S$	$5.5 \pm 0.2 R_S$	$7 \pm 0.2 R_S$
A_i	1.22 ± 0.75	1.02 ± 0.69	0.40 ± 0.20	0.22 ± 0.15
B_i	-9.94 ± 24.9	32.4 ± 23.0	36.3 ± 6.62	15.1 ± 4.82
A_e	1.28 ± 0.42	0.89 ± 0.28	0.11 ± 0.14	0.12 ± 0.04
B_e	-8.91 ± 13.9	37.9 ± 9.33	42.9 ± 4.76	14.6 ± 1.43

Note. The coefficients are given with 95% confidence intervals.

The figure clearly shows how the dependence is decreasing for increasing distances from Saturn. This is even more clear in Figure 9 (fifth panel) that shows all fits from the four different distances starting at 0 cm^{-3} , the line styles (dotted, dashed, etc.), correspond to the styles used in Figure 9 (first to fourth panels). The density variation decreases from around 30 cm^{-3} at $3.5 R_S$ to around 0 cm^{-3} at $7 R_S$. Figure 9 also shows how fluctuations in the plasma density are increasing with decreasing distance to Saturn, showing how dynamic the inner part of the plasma disk is. The good agreement between n_e and the LP n_i for the different distances, despite being measured by two different instruments, and the LP n_i presented as the median value for each year and the n_e presented as the average over each 6 months, is a strong indicator of the good accuracy of both measurement techniques.

3.4. Cold Plasma Dayside/Nightside Density Asymmetry

Schippers et al. (2013) and Holmberg et al. (2014) showed that the equatorial plasma density varies with LT within $10 R_S$. Both studies showed a dayside/nightside asymmetry, and Holmberg et al. (2014) suggested that the asymmetry is due to a shift of the whole plasma disk toward LT noon. The shift would be related to the previously detected drift, toward noon, of energetic electron microsignatures, studied by Roussos et al. (2007) and Andriopoulou et al. (2012). Andriopoulou et al. (2012) suggested that the drift is due to a global noon-to-midnight-directed electric field of about 0.1 mV/m superimposed on the (sub)corotation electric field. Wilson et al. (2013) showed that the drift is also present in the cold plasma population as an asymmetry in the radial velocity component. Another possible cause of the plasma density dayside/nightside asymmetry is a dayside/nightside asymmetry in the ion temperature. For constant flux tube content, colder ion temperatures on the nightside result in shorter density scale heights and thus higher densities in the equatorial plane. However, Thomsen et al. (2012) detected the opposite, that is, a slightly larger nightside ion temperature than dayside temperature. Hence, the ion temperature LT asymmetry cannot explain the detected plasma density LT asymmetry.

Figure 10 shows that a density difference, of a factor of ~ 2 , also can be found in our extended data set. The difference is largest in the region between 4 and $5 R_S$. Figure 10 shows the median ion density, for each $0.5 R_S$ bin, divided into a dayside LT $12 \pm 3 \text{ h}$ (red) and a nightside LT $00 \pm 3 \text{ h}$ (black). The presented data set is limited to the equator plane, $|z| < 0.25 R_S$.

The measured ion density difference does not change noticeably when using a narrower region, down to $|z| < 0.05 R_S$, which shows that a possibly interfering dayside/nightside Z asymmetry can be ruled out. The median ion density in between 4 and $5 R_S$ is consistently larger for LT $00 \pm 3 \text{ h}$ than for LT $12 \pm 3 \text{ h}$, throughout the mission (not shown). The radial distance between the dayside and nightside median ion density peaks is about $0.5 R_S$, which corresponds well to the radial offset of 0.5 to $1 R_S$ derived by Thomsen et al. (2012) for the dayside/nightside asymmetry found in CAPS plasma ion and electron temperatures and energetic particle phase space densities.

Figure 10 shows larger nightside ion densities all the way out to around $9 R_S$. This is not in agreement with the n_e LT asymmetry presented by Schippers et al. (2013). They used RPWS n_e measurements from July 2004 to May 2012. Schippers et al. (2013) showed higher electron densities for the nightside LT $00 \pm 5 \text{ h}$ than for the dayside LT $12 \pm 5 \text{ h}$ out to $\sim 5 R_S$.

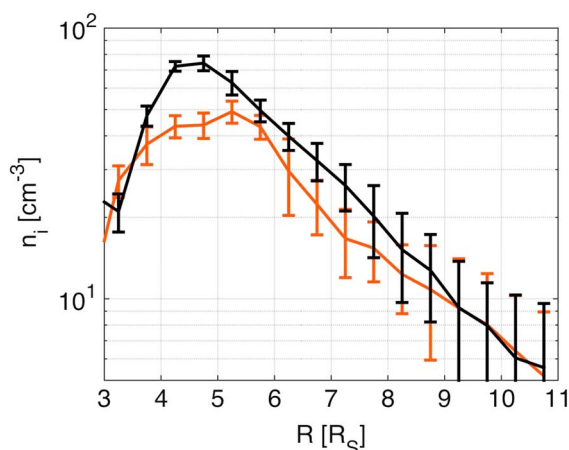


Figure 10. Median values of the equatorial, $|z| < 0.25 R_S$, ion density measured at LT $12 \pm 3 \text{ h}$ (red) and LT $00 \pm 3 \text{ h}$ (black) from orbit 3 to 237.

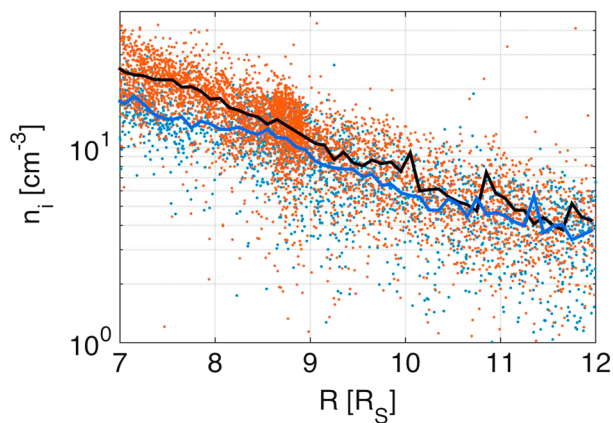


Figure 11. Equatorial, $|z| < 0.25 R_S$, ion density divided into two subsets: (1) Sun-ring plane angle $\theta_{SR} > 18^\circ$ (blue dots), median value for each $0.1 R_S$ (black line) and (2) $\theta_{SR} < 8^\circ$ (red dots), median value for each $0.1 R_S$ (blue line). No interference from the magnetodisc flapping can be found in the LP n_i measurements for $R < 12 R_S$.

and higher dayside densities from $\sim 6.5 R_S$ and outward, a factor of 2 larger. This is not shown in the LP n_i subset presented in Figure 10. For the same subset as used in Schippers et al. (2013) the LP n_i shows slightly larger dayside n_i for $R > 9 R_S$ (not shown). The cause of the disagreement is still unknown and under investigation.

A similar asymmetry as the presented dayside/nightside asymmetry is not found in the LP n_i , nor in the n_e , when comparing dawn/dusk measurements.

3.5. Influence of the Flapping Magnetodisc

One potential interference that could affect the shown dayside/nightside asymmetry is the flapping of the magnetodisc. As has been discussed and shown in section 2 the flapping of the magnetodisc can clearly be seen in the measurements performed in the outer magnetosphere. Khurana et al. (2009) showed that the effect of the flapping magnetodisc could be detected in measurements of the radial component of the magnetic field as close to Saturn as $5 R_S$, their Figure 8. Khurana et al. (2009) also suggested that the flapping of the magnetodisc is due to the solar wind pushing the azimuthally asymmetric plasma disk from below. Assuming this to

be the origin of the magnetodisc flapping, a potential effect in the LP equatorial n_i measurements should be possible to detect simply by dividing the data set into two subsets, one for large Sun declination angle and one for small. For larger/smaller Sun declination angle the magnetodisc would be more/less deflected away from the equatorial plane and the median of the measured equatorial n_i should be smaller/larger.

Figure 11 shows the 11 year data set divided into two subsets, one for Sun-ring plane angle $26.7^\circ > \theta_{SR} > 18^\circ$ and one for $8^\circ > \theta_{SR} > 0^\circ$, plotted against R for $R > 7 R_S$. Figure 11 shows slightly larger/smaller densities, $\Delta n_i < 8 \text{ cm}^{-3}$, for larger/smaller θ_{SR} , and Δn_i is decreasing with increasing radial distance R . If the flapping of the magnetodisc could have been detected at these small radial distances, Figure 11 would have shown the opposite result. We can therefore conclude that the magnetodisc flapping does not affect the LP n_i measurements at the radial distances studied in this article. The Δn_i that is detected within about $10 R_S$ is, most probably, due to the plasma disk density varying with the varying EUV flux, as was discussed in section 3.3.

4. Conclusions

We use a new and improved data analysis method to derive ion density from the Cassini LP measurements recorded during the time interval from orbit 3 (1 February 2005) to 237 (29 June 2016) and in the radial region between 2.5 and $12 R_S$. We show that the LP measurements are affected both by the previously detected flapping of the magnetodisc (Figure 1) and the wake formation of Cassini (Figure 2). A possible interference in the LP n_i measurements within $12 R_S$ due to the flapping of the magnetodisc was studied, and no such influence was detected. However, at larger distances the interference is significant and must be taken into consideration. Measurements performed in the Cassini spacecraft wake have been excluded from the data presented in this article.

The measured n_i displays a more continuous plasma disk than previously reported (Figure 3), with a median density given by equation (11) where the plasma disk peak density $n_0 = 64.9 \text{ cm}^{-3}$ is found at distance $R_0 = 4.47 R_S$, and the radial dependences are given by $c = 6.66$, and $d = 3.79$. The derived median ion density agrees very well with the electron density derived from the f_{UHR} , usually within 3 cm^{-3} with a maximum difference of 6 cm^{-3} outside of $4.2 R_S$ (Figure 4), which is a good confirmation of the accuracy of both measurement techniques. The LP median n_i also agrees well with CAPS data within $5 R_S$ presented by Livi et al. (2014) (Figure 4), which is an interesting result that needs further investigation since n_e from f_{UHR} shows larger densities inside $4.2 R_S$. The difference is suggested to be due to cluster ions that are present to a larger degree within the orbit of Enceladus and that may interfere with the LP measurements. The suggested explanation for the detected difference between n_e and LP n_i within $4.2 R_S$ is currently being studied.

It is shown that the plasma disk density maximum is located at around $4.6 R_S$, that is, shifted from the neutral source region, Enceladus, by around $0.6 R_S$, when excluding measurements recorded in the close vicinity of Enceladus. This is clearly seen in all three data sets compared in Figure 4: the RPWS/LP n_i , the RPWS n_e ,

and the CAPS n_i . The shift can be explained by the hot electron impact ionization being an important ionization process in this region. The hot (>12.6 eV) electron density n_{eh} from four Cassini orbits and measured by CAPS ELS is presented in Figure 5. The peak of the n_{eh} is about 1.2 cm^{-3} and located at around $7 R_S$. As new ions are produced by hot electron impact ionization the production peak will be located in between the neutral density peak (at around $3.95 R_S$) and the n_{eh} peak. An analogy to this is the altitude of the peak plasma density of any ionosphere, which is given by the altitude-dependent neutral density and intensity of the ionizing radiation (Chapman, 1931).

We also study the solar cycle and seasonal modulations of the plasma disk. Tseng et al. (2010) predicted that the plasma density within $2.5 R_S$ should show a seasonal variation, assuming that photodissociation of ring particles is the main source of O_2 , and subsequent photoionization resulting in O_2^+ , in this region. Elrod et al. (2012, 2014) showed that the CAPS ion density shows a seasonal modulation in the region 2.4 to $3.5 R_S$, and this was also found in the RPWS n_e (Persoon et al., 2015). However, the change in insolation angle before the year 2015 follows the change that would be detected due to the changing solar EUV flux. It is therefore difficult to measure the importance of seasonal changes versus solar cycle, as was also discussed by Elrod et al. (2012, 2014) and Persoon et al. (2015). The RPWS n_e and LP n_i measurements from 2016, presented in this paper, show a much better correlation with the solar cycle modulation than with the seasonal variation, Figures 6 to 9. Estimates including the photoionization, hot electron impact ionization, and loss by transport show a maximum density variation $\Delta n_i \approx 20 \text{ cm}^{-3}$, and the measurements show a density drop of $\sim 25 \text{ cm}^{-3}$. The density decrease of $\sim 25 \text{ cm}^{-3}$ is larger than expected since the insolation angle for 2016 is large which provides an increase in density due to the larger amount of O_2^+ origin from the main rings. The density increase from the large insolation angle and the density decrease due to lower F_{EUV} were expected to produce a smaller density decrease than the measured one. This could imply that an additional unknown source process, also EUV dependent, is also affecting the plasma density in the inner part of the plasma disk. The measurement results from the 2017 orbits will be the key in deriving the importance of seasonal versus solar cycle dependences, since the insolation angle still will be large (corresponding to large n_i) and the EUV flux even lower than in 2016 (corresponding to low n_i).

Assuming that the ring plasma continues to demonstrate a seasonal dependency, a likely prediction for the 2017 measurements is that the innermost part of the plasma disk, within about $2.7 R_S$, will show large density values due to the increase in O^+ production as the insolation angle is large and the number of photons for each unit area of the inner rings will be larger. The region around Enceladus, around 2.7 to $6 R_S$, however, will show a lower density than in 2016 since the solar cycle will be approaching its minimum and the solar EUV flux will be lower.

A discussion about the previously detected dayside/nightside asymmetry of the cold plasma (Holmberg et al., 2014; Schippers et al., 2013) is presented. We show that the asymmetry also can be detected in the extended data set presented in this paper. The asymmetry has previously been suggested to be due to a shift of the whole plasma disk toward LT noon. A density difference, of around a factor of 2, is found in the region between 4 and $5 R_S$ (Figure 10). The radial distance between the dayside and the nightside median ion density peak is about $0.5 R_S$, which corresponds well to the dayside/nightside radial offset of 0.5 to $1 R_S$ detected in the CAPS ion and electron temperatures and energetic particle phase space densities (Thomsen et al., 2012). No asymmetry was found when comparing dawn/dusk n_i measurements.

References

- André, N., Dougherty, M. K., Russell, C. T., Leisner, J. S., & Khurana, K. K. (2005). Dynamics of the Saturnian inner magnetosphere: First inferences from the Cassini magnetometers about small-scale plasma transport in the magnetosphere. *Geophysical Research Letters*, *32*, L14506. <https://doi.org/10.1029/2005GL022643>
- Andriopoulou, M., Roussos, E., Krupp, N., Paranicas, C., Thomsen, M., Krimigis, S., ... Glassmeier, K.-H. (2012). A noon-to-midnight electric field and nightside dynamics in Saturn's inner magnetosphere, using microsignature observations. *Icarus*, *220*(2), 503–513.
- Brace, L. H., Hoegy, W. R., & Theis, R. F. (1988). Solar EUV measurements at Venus based on photoelectron emission from the Pioneer Venus Langmuir probe. *Journal of Geophysical Research*, *93*(A7), 7282–7296.
- Burch, J. L., Goldstein, J., Hill, T. W., Young, D. T., Crary, F. J., Coates, A. J., ... Sittler Jr., E. C. (2005). Properties of local plasma injections in Saturn's magnetosphere. *Geophysical Research Letters*, *32*, L14502. <https://doi.org/10.1029/2005GL022611>
- Cairns, R. B., & Samson, J. A. R. (1966). Metal photocathodes as secondary standards for absolute intensity measurements in the vacuum ultraviolet. *Journal of the Optical Society of America*, *56*(11), 1568–1573.
- Chapman, S. (1931). The absorption and dissociative or ionizing effect of monochromatic radiation in an atmosphere on a rotating earth. *Proceedings of the Physical Society*, *43*(1), 26–45.
- Chen, Y., Liu, L., & Wan, W. (2011). Does the $F_{10.7}$ index correctly describe solar EUV flux during the deep solar minimum of 2007–2009? *Journal of Geophysical Research*, *116*, A04304. <https://doi.org/10.1029/2010JA016301>

Acknowledgments

The Cassini RPWS/LP data are available at the University of Iowa and the Swedish Institute of Space Physics. The Swedish National Space Board (SNSB) supports the RPWS/LP instrument on board Cassini. The ion density data set presented in this article is available on the Automated Multi-Dataset Analysis (AMDA) tool at <http://amda.cdpp.eu>, developed by the French Plasma Physics Data Center (CDPP) (<http://www.cdpp.eu/>). The authors would like to thank the CDPP/AMDA team for the integration of this data set and for providing the spacecraft potential presented in Figure 1. The CDPP is supported by the CNRS, CNES, Observatoire de Paris, and Université Paul Sabatier, Toulouse. The spacecraft potential is also available at the Planetary Plasma Interaction (PPI) Node of the Planetary Data System (PDS), in the files RPWS_LP_NEPROXY_2006289_V1 to RPWS_LP_NEPROXY_2006294_V1. The TIMED/SEE and SORCE/SOLSTICE data are available at <http://lasp.colorado.edu/lisird/>. The CAPS ELS data are available at the Mullard Space Science Laboratory. O. S. acknowledges funding from the SNSB under contract Dnr 130/11:2. E. V. acknowledges funding from the SNSB under contract Dnr 166/14.

- Dougherty, M. K., Khurana, K. K., Neubauer, F. M., Russell, C. T., Saur, J., Leisner, J. S., & Burton, M. E. (2006). Identification of a dynamic atmosphere at Enceladus with the Cassini magnetometer. *Science*, *311*(5766), 1406–1409.
- Elrod, M. K., Tseng, W.-L., Wilson, R. J., & Johnson, R. E. (2012). Seasonal variations in Saturn's plasma between the main rings and Enceladus. *Journal of Geophysical Research*, *117*, A03207. <https://doi.org/10.1029/2011JA017332>
- Elrod, M. K., Tseng, W.-L., Woodson, A. K., & Johnson, R. E. (2014). Seasonal and radial trends in Saturn's thermal plasma between the main rings and Enceladus. *Icarus*, *242*, 130–137.
- Engwall, E., Eriksson, A. I., Cully, C. M., André, M., Puhl-Quinn, P. A., Vaith, H., & Torbert, R. (2009). Survey of cold ionospheric outflows in the magnetotail. *Annales Geophysicae*, *27*, 3185–3201.
- Fahleson, U. (1967). Theory of electric field measurements conducted in the magnetosphere with electric probes. *Space Science Reviews*, *7*, 238–262.
- Fleshman, B. L., Delamere, P. A., & Bagenal, F. (2010). A sensitivity study of the Enceladus torus. *Journal of Geophysical Research*, *115*, E04007. <https://doi.org/10.1029/2009JE003372>
- Fleshman, B. L., Delamere, P. A., Bagenal, F., & Cassidy, T. (2013). A 1-D model of physical chemistry in Saturn's inner magnetosphere. *Journal of Geophysical Research: Planets*, *118*, 1567–1581. <https://doi.org/10.1002/jgre.20106>
- Garnier, P., Holmberg, M. K. G., Wahlund, J.-E., Lewis, G. R., Grimald, S. R., Thomsen, M. F., ... Dandouras, I. (2013). The influence of the secondary electrons induced by energetic electrons impacting the Cassini Langmuir probe at Saturn. *Journal of Geophysical Research: Space Physics*, *118*, 7054–7073. <https://doi.org/10.1002/2013JA019114>
- Garnier, P., Holmberg, M. K. G., Wahlund, J.-E., Lewis, G. R., Schippers, P., Coates, A., ... Dandouras, I. (2014). Deriving the characteristics of warm electrons (100–500 eV) in the magnetosphere of Saturn with the Cassini Langmuir probe. *Planetary and Space Science*, *104*, 173–184.
- Garnier, P., Wahlund, J.-E., Holmberg, M. K. G., Morooka, M., Grimald, S., Eriksson, A., ... Gustafsson, G. (2012). The detection of energetic electrons with the Cassini Langmuir probe at Saturn. *Journal of Geophysical Research*, *117*, A10202. <https://doi.org/10.1029/2011JA017298>
- Girazian, Z., & Withers, P. (2013). The dependence of peak electron density in the ionosphere of Mars on solar irradiance. *Geophysical Research Letters*, *40*, 1960–1964. <https://doi.org/10.1002/grl.50344>
- Gurnett, D. A., Kurth, W. S., Kirchner, D. L., Hospodarsky, G. B., Averkamp, T. F., Zarka, P., ... Pedersen, A. (2004). The Cassini radio and plasma wave investigation. *Space Science Reviews*, *114*, 395–463.
- Gurnett, D. A., Kurth, W. S., Hospodarsky, G. B., Persoon, A. M., Averkamp, T. F., Cecconi, B., ... Pedersen, A. (2005). Radio and plasma wave observations at Saturn from Cassini's approach and first orbit. *Science*, *307*(5713), 1255–1259.
- Gustafsson, G., & Wahlund, J.-E. (2010). Electron temperatures in Saturn's plasma disc. *Planetary and Space Science*, *58*(7–8), 1018–1025.
- Hill, T. W., Rymer, A. M., Burch, J. L., Cray, F. J., Young, D. T., Thomsen, M. F., ... Lewis, G. R. (2005). Evidence for rotationally driven plasma transport in Saturn's magnetosphere. *Geophysical Research Letters*, *32*, L14510. <https://doi.org/10.1029/2005GL022620>
- Holmberg, M. K. G., Wahlund, J.-E., & Morooka, M. W. (2014). Dayside/nightside asymmetry of ion densities and velocities in Saturn's inner magnetosphere. *Geophysical Research Letters*, *41*, 3717–3723. <https://doi.org/10.1002/2014GL060229>
- Holmberg, M. K. G., Wahlund, J.-E., Morooka, M. W., & Persoon, A. M. (2012). Ion densities and velocities in the inner plasma torus of Saturn. *Planetary and Space Science*, *73*, 151–160.
- Holmberg, M. K. G., Wahlund, J.-E., Vigren, E., Cassidy, T. A., & Andrews, D. J. (2016). Transport and chemical loss rates in Saturn's inner plasma disk. *Journal of Geophysical Research: Space Physics*, *121*, 2321–2334. <https://doi.org/10.1002/2015JA021784>
- Huebner, W. F., & Carpenter, C. W. (1979). Solar photo rate coefficients (Report LA-8085-MS). Los Alamos, New Mexico: Los Alamos Scientific Laboratory.
- Huebner, W. F., Keady, J. J., & Lyon, S. P. (1992). Solar photo rates for planetary atmospheres and atmospheric pollutants. *Astrophysics and Space Science*, *195*(1), 1–294.
- Huebner, W. F., & Mukherjee, J. (2015). Photoionization and photodissociation rates in solar and blackbody radiation fields. *Planetary and Space Science*, *106*, 11–45.
- Jacobsen, K. S., Wahlund, J.-E., & Pedersen, A. (2008). Cassini Langmuir probe measurements in the inner magnetosphere of Saturn. *Planetary and Space Science*, *57*, 48–52.
- Jia, X., & Kivelson, M. G. (2012). Driving Saturn's magnetospheric periodicities from the upper atmosphere/ionosphere: Magnetotail response to dual sources. *Journal of Geophysical Research*, *117*, A11219. <https://doi.org/10.1029/2012JA018183>
- Khurana, K. K., Mitchell, D. G., Arridge, C. S., Dougherty, M. K., Russell, C. T., Paranicas, C., ... Coates, A. J. (2009). Sources of rotational signals in Saturn's magnetosphere. *Journal of Geophysical Research*, *114*, A02211. <https://doi.org/10.1029/2008JA013312>
- Lazarus, A. J., & McNutt Jr., R. L. (1983). Low-energy plasma ion observations in Saturn's magnetosphere. *Journal of Geophysical Research*, *88*(A11), 8831–8846.
- Lewis, G. R., André, N., Arridge, C. S., Coates, A. J., Gilbert, L. K., Linder, D. R., & Rymer, A. M. (2008). Derivation of density and temperature from the Cassini-Huygens CAPS electron spectrometer. *Planetary and Space Science*, *56*(7), 901–912.
- Livi, R. J., Goldstein, J., Burch, J. L., Cray, F., Rymer, A. M., Mitchell, D. G., & Persoon, A. M. (2014). Multi-instrument analysis of plasma parameters in Saturn's equatorial, inner magnetosphere using corrections for spacecraft potential and penetrating background radiation. *Journal of Geophysical Research: Space Physics*, *119*, 3683–3707. <https://doi.org/10.1002/2013JA019616>
- Menietti, J. D., Santolík, O., Rymer, A. M., Hospodarsky, G. B., Persoon, A. M., Gurnett, D. A., ... Young, D. T. (2008). Analysis of plasma waves observed within local plasma injections seen in Saturn's magnetosphere. *Journal of Geophysical Research*, *113*, A05213. <https://doi.org/10.1029/2007JA012856>
- Miloch, W. J., Yaroshenko, V. V., Vladimirov, S. V., Pécseli, H. L., & Trulsen, J. (2012). Spacecraft charging in flowing plasmas: Numerical simulations. *Journal of Physics: Conference Series*, *370*(1), 012004.
- Moncuquet, M., Lecacheux, A., Meyer-Vernet, N., Cecconi, B., & Kurth, W. S. (2005). Quasi thermal noise spectroscopy in the inner magnetosphere of Saturn with Cassini/RPWS: Electron temperatures and density. *Geophysical Research Letters*, *32*, L20502. <https://doi.org/10.1029/2005GL022508>
- Morooka, M. W., Modolo, R., Wahlund, J.-E., André, M., Eriksson, A. I., Persoon, A. M., ... Dougherty, M. (2009). The electron density of Saturn's magnetosphere. *Annales Geophysicae*, *27*, 2971–2991.
- Morooka, M. W., Wahlund, J.-E., Eriksson, A. I., Farrell, W. M., Gurnett, D. A., Kurth, W. S., ... Holmberg, M. K. G. (2011). Dusty plasma in the vicinity of Enceladus. *Journal of Geophysical Research*, *116*, A12221. <https://doi.org/10.1029/2011JA017038>
- Orient, O. J., & Strivastava, S. K. (1987). Electron impact ionisation of H₂O, CO, CO₂ and CH₄. *Journal of Physics B*, *20*(15), 3923–3936.
- Persoon, A. M., Gurnett, D. A., Kurth, W. S., Groene, J. B., & Faden, J. B. (2015). Evidence for a seasonally dependent ring plasma in the region between Saturn's A Ring and Enceladus' orbit. *Journal of Geophysical Research: Space Physics*, *120*, 6276–6285. <https://doi.org/10.1002/2015JA021180>

- Persoon, A. M., Gurnett, D. A., Kurth, W. S., Hospodarsky, G. B., Groene, J. B., Canu, P., & Dougherty, M. K. (2005). Equatorial electron density measurements in Saturn's inner magnetosphere. *Geophysical Research Letters*, *32*, L23105. <https://doi.org/10.1029/2005GL024294>
- Persoon, A. M., Gurnett, D. A., Leisner, J. S., Kurth, W. S., Groene, J. B., & Faden, J. B. (2013). The plasma density distribution in the inner region of Saturn's magnetosphere. *Journal of Geophysical Research: Space Physics*, *118*, 2970–2974. <https://doi.org/10.1002/jgra.50182>
- Persoon, A. M., Gurnett, D. A., Santolik, O., Kurth, W. S., Faden, J. B., Groene, J. B., ... Moncuquet, M. (2009). A diffusive equilibrium model for the plasma density in Saturn's magnetosphere. *Journal of Geophysical Research*, *114*, A04211. <https://doi.org/10.1029/2008JA013912>
- Porco, C. C., Helfenstein, P., Thomas, P. C., Ingersoll, A. P., Wisdom, J., West, R., ... Squyres, S. (2006). Cassini observes the active south pole of Enceladus. *Science*, *311*(5766), 1393–1401.
- Roussos, E., Jones, G. H., Krupp, N., Paranicas, C., Mitchell, D. G., Lagg, A., ... Dougherty, M. K. (2007). Electron microdiffusion in the Saturnian radiation belts: Cassini MIMI/LEMMS observations of energetic electron absorption by the icy moons. *Journal of Geophysical Research*, *112*, A06214. <https://doi.org/10.1029/2006JA012027>
- Rymer, A. M., Mauk, B. H., Hill, T. W., Paranicas, C., Mitchell, D. G., Coates, A. J., & Young, D. T. (2008). Electron circulation in Saturn's magnetosphere. *Journal of Geophysical Research*, *113*, A01201. <https://doi.org/10.1029/2007JA012589>
- Schippers, P., Blanc, M., André, N., Dandouras, I., Lewis, G. R., Gilbert, L. K., ... Dougherty, M. K. (2008). Multi-instrument analysis of electron populations in Saturn's magnetosphere. *Journal of Geophysical Research*, *113*, A07208. <https://doi.org/10.1029/2008JA013098>
- Schippers, P., Moncuquet, M., Meyer-Vernet, N., & Lecacheux, A. (2013). Core electron temperature and density in the innermost Saturn's magnetosphere from HF power spectra analysis on Cassini. *Journal of Geophysical Research: Space Physics*, *118*, 7170–7180. <https://doi.org/10.1002/2013JA019199>
- Sittler Jr., E. C., André, N., Blanc, M., Burger, M., Johnson, R. E., Coates, A., ... Young, D. T. (2008). Ion and neutral sources and sinks within Saturn's inner magnetosphere: Cassini results. *Planetary and Space Science*, *56*(1), 3–18.
- Sittler Jr., E. C., Ogilvie, K. W., & Scudder, J. D. (1983). Survey of low-energy plasma electrons in Saturn's magnetosphere: Voyagers 1 and 2. *Journal of Geophysical Research*, *88*(A11), 8847–8870.
- Sittler Jr., E. C., Thomsen, M., Johnson, R. E., Hartle, R. E., Burger, M., Chornay, D., ... André, N. (2006). Cassini observations of Saturn's inner plasmasphere: Saturn orbit insertion results. *Planetary and Space Science*, *54*(12), 1197–1210.
- Thomsen, M. F. (2013). Saturn's magnetospheric dynamics. *Geophysical Research Letters*, *40*, 5337–5344. <https://doi.org/10.1002/2013GL057967>
- Thomsen, M. F., Reisenfeld, D. B., Delapp, D. M., Tokar, R. L., Young, D. T., Cray, F. J., ... Williams, J. D. (2010). Survey of ion plasma parameters in Saturn's magnetosphere. *Journal of Geophysical Research*, *115*, A10220. <https://doi.org/10.1029/2010JA015267>
- Thomsen, M. F., Roussos, E., Andriopoulou, M., Kollmann, P., Arridge, C. S., Paranicas, C. P., ... Young, D. T. (2012). Saturn's inner magnetospheric convection pattern: Further evidence. *Journal of Geophysical Research*, *117*, A09208. <https://doi.org/10.1029/2010JA015267>
- Tseng, W.-L., Ip, W.-H., Johnson, R. E., Cassidy, T. A., & Elrod, M. K. (2010). The structure and time variability of the ring atmosphere and ionosphere. *Icarus*, *206*(2), 382–389.
- Wahlund, J.-E., Boström, R., Gustafsson, G., Gurnett, D. A., Kurth, W. S., Averkamp, T., ... André, M. (2005). The inner magnetosphere of Saturn: Cassini RPWS cold plasma results from the first encounter. *Geophysical Research Letters*, *32*, L20509. <https://doi.org/10.1029/2005GL022699>
- Wilson, R. J., Bagenal, F., Delamere, P. A., Desroche, M., Fleshman, B. L., & Dols, V. (2013). Evidence from radial velocity measurements of a global electric field in Saturn's inner magnetosphere. *Journal of Geophysical Research: Space Physics*, *118*, 2122–2132. <https://doi.org/10.1002/jgra.50251>
- Young, D. T., Berthelier, J.-J., Blanc, M., Burch, J. L., Bolton, S., Coates, A. J., ... Zinsmeyer, C. (2005). Composition and dynamics of plasma in Saturn's magnetosphere. *Science*, *307*(5713), 1262–1266.
- Young, D. T., Berthelier, J.-J., Blanc, M., Burch, J. L., Coates, A. J., Goldstein, R., ... Zinsmeyer, C. (2004). Cassini plasma spectrometer investigation. *Space Science Reviews*, *114*, 1–112.